JOURNAL OF AIRCRAFT
Vol. 45, No. 2, March–April 2008

Uniformly High-Order Essentially Nonoscillatory Schemes for Vortex Convection Across Overset Interfaces

Nathan Hariharan*
United Technologies Research Center,
East Hartford, Connecticut 06066
and
Lakshmi Sankar†
Georgia Institute of Technology,
Atlanta, Georgia 30332

DOI: 10.2514/1.31477

The construction of uniformly high-order accurate numerical schemes based on an essentially nonoscillatory methodology was considered in this work. In particular, the accuracy of essentially nonoscillatory scheme implementations near the interface boundaries for overset grids was analyzed. Essentially nonoscillatory schemes use large stencil support for constructing progressively high-order spatial accuracy schemes. The handling of such schemes near overset boundaries influences the overall solution accuracy for large-scale computations. An essentially nonoscillatory based fifth/seventh-order spatially accurate Euler/Navier–Stokes overset solver was used to study the convection of vortices across overset interfaces. Three different numerical formulations near the boundary interfaces were constructed, and their ability to preserve high-order solution accuracy near the overset interface boundaries was studied. Two overlapping Cartesian meshes were generated, and a Lamb's vortex was convected across the overset interface between the two meshes. The fidelity of the vortex as it crossed the interface was analyzed, and the results were compared for the three near-boundary formulations. It was found that the preservation of the vortex strength crucially depended upon the correct formulation and interpolation of high-order fluxes within the essentially nonoscillatory framework near the overset interface.

Nomenclature

$\|A\|$	=	Roe's dissipation matrix
$A(\cdot)$, $E(\cdot)$, $R(\cdot)$	=	Operators
C_T	=	thrust coefficient
F	=	flux vector for inviscid fluxes
F_v	=	flux vector for viscous fluxes
$\boldsymbol{i}$, $\boldsymbol{j}$, $\boldsymbol{k}$	=	Cartesian directional unit vectors
M_{tip}	=	tip Mach number (for rotor blade)
M_∞	=	freestream Mach number
q	=	vector of primitive flow variables
q_L	=	left-hand side flow vector at a given face
q_R	=	right-hand side flow vector at a given face
R	=	rotor disk radius
V_F	=	fluid velocity
V_G	=	grid velocity
v_i	=	induced velocity
α	=	angle of attack
ΔS	=	face surface area
λ	=	advance ratio
ξ, η, ζ	=	structured grid generalized coordinate directions
τ	=	time
Ω	=	rotor angular velocity
Ω_J	=	cell volume

Presented as Paper 1263 at the 43rd AIAA Aerospace Sciences Meeting and Exhibit, Reno, Nevada, 10–13 January 2005; received 9 April 2007; revision received 26 October 2007; accepted for publication 28 October 2007.

*Staff Engineer, 411 Silver Lane.
†Regents Professor, School of Aerospace Engineering, 270 Ferst Drive.

I. Introduction

THE flowfield around a rotor, whether in forward flight or hover, is difficult to model due to the presence of strong vorticity. The flow phenomena for a rotor differ from those of a wing in forward flight, because of the differing influence of their respective wakes. For a wing in forward flight, the generated tip vortex and the vortex sheet are quickly convected away from the wing, and the influence of the shed wake on the flowfield in the vicinity of the wing is small. For an adequate numerical simulation of a wing in forward flight, it is sufficient to capture the generated tip vortex in the vicinity of the wing. In contrast, in the flowfield around a rotor, a strong vortex wake system lingers in the vicinity of the rotor. In hover, the wake vortex coils beneath the rotor and significantly alters the effective angle of attack of the rotor.

Accurate numerical prediction of rotor-blade aerodynamic parameters such as thrust coefficient and induced torque coefficient requires an accurate modeling of the wake vortex. In forward flight the entire vortex system is swept back, leading to strong interactions between the blade-tip vortices and the successive blades, a phenomenon known as the blade-vortex interaction (BVI). These blade-vortex interactions result in rapid changes in local flow conditions and are a major source of aerodynamic noise and structural vibration.

The underlying issue in modeling rotorcraft aerodynamics is the necessity to fully account for the complex vortex system generated by the rotor blades. Researchers in the past two decades have adopted a broad class of methodologies with various levels of complexity to model the vortex system. Until recently, this representation was externally input from empirical/analytical models because full Euler/Navier–Stokes (NS) computations were infeasible. With the enormous advances in computational methodologies and computational power, researchers have been adapting Euler/NS techniques for the study of the rotor flowfield. These solvers are particularly useful in analyzing new or complex rotor blades for which no experimental data is available. Studies by Srinivasan and Ahmad [1], Strawn and Barth [2], and Duque [3,4] have used a variety of strategies such as unstructured methodologies and overset

methodologies to tackle this problem. An excellent survey paper by McCroskey [5] gives a comprehensive review of modern computational strategies for rotor applications.

Such methodologies that solve for the flowfield from the basic conservation laws without using additional information (information from analyses such as other numerical formulations, analytical formulations, or experimental observations) are generally referred to as "first principles"-based methods. Traditional low-order spatially accurate Euler/Navier–Stokes computational methodologies tend to dissipate the vortex wake system due to the high numerical dissipation built into such numerical schemes [5]. Some amount of dissipation is essential for numerical schemes to damp high-frequency oscillations. However, such a procedure should not diffuse legitimate flow features, such as vorticity, that exhibit sharp gradients in flow properties.

Essentially nonoscillatory (ENO) schemes developed by Shu and Osher [6,7] and Harten et al. [8] offer an elegant approach to constructing high-order accurate, low-dissipation numerical schemes. One of the earliest, relatively successful attempts by Hariharan and Sankar [9,10] to capture three-dimensional rotary-wing vortex wakes used the ENO methodology. In recent years, various other approaches to building high-order schemes for rotor wake capturing have also been proposed. Schemes such as dispersion relation preserving schemes [11] and projected monotone upstream-centered schemes for conservation laws[12] have been tried out for studying rotorcraft wakes with varying degrees of success. Compact high-order schemes, or schemes that use information only from any given cell and its neighbors, such as discontinuous Galerkin [13], have been moderately successful for three-dimensional unsteady vortex capturing so far. More research is needed to refine high-order methods further to arrive at an optimal scheme applicable for three-dimensional calculations.

This paper focuses specifically upon the use of fifth/seventh-order spatially accurate, essentially nonoscillatory schemes for capturing vortices while minimizing numerical dissipation. One of the drawbacks of ENO schemes is that they are not compact, and hence a wide stencil of information is required to construct the high-fidelity solution. This becomes a problem when large-scale simulations are broken into parts and distributed over a computing network, making it necessary to have sufficient overlap between the grid parts to construct a uniformly high-order accurate solution. One possible solution is to let the adaptive underlying methodology of ENO

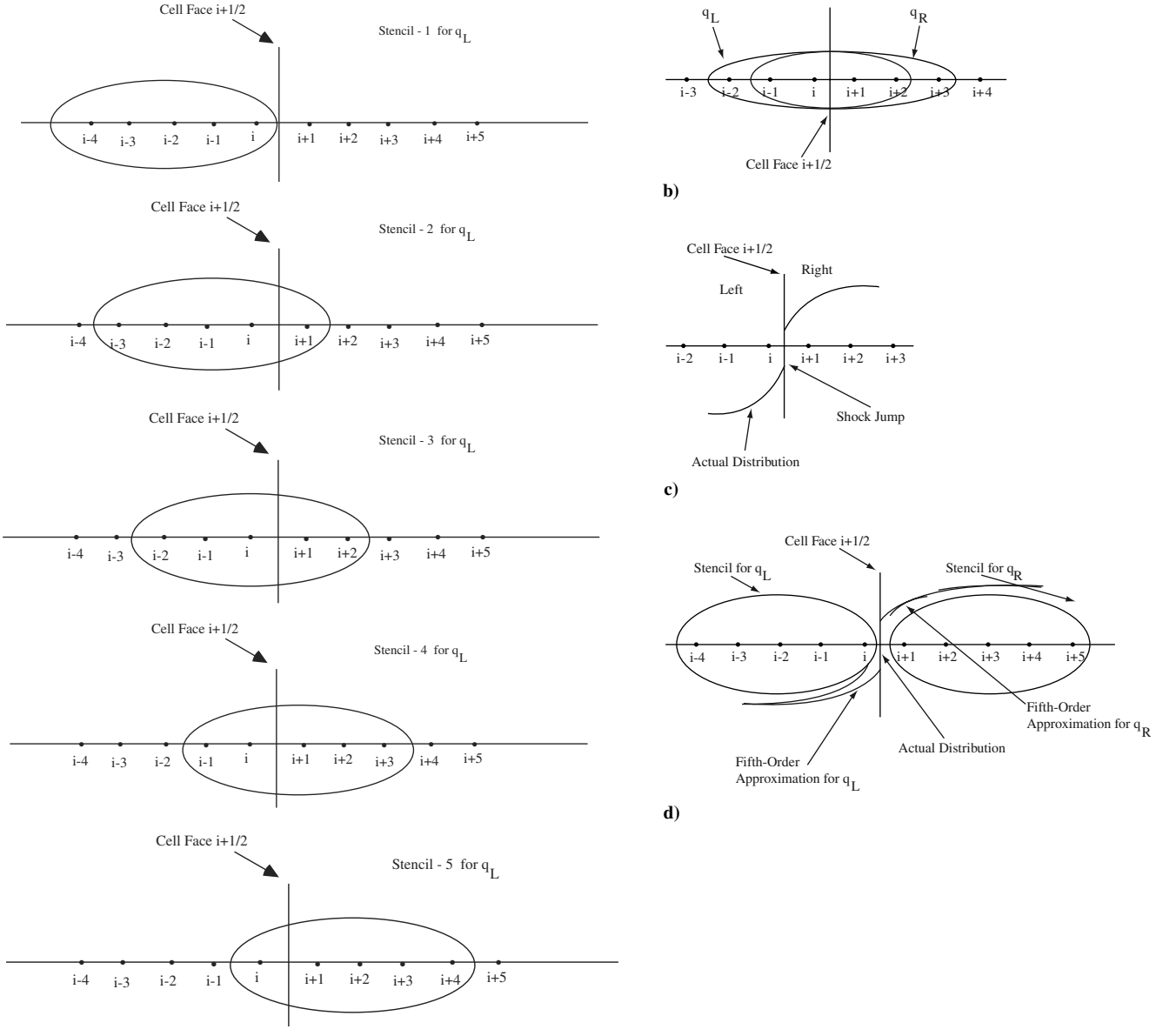

Fig. 1 Stencil support for ENO projection: a) schematic of five possible q_L stencils for the fifth-order scheme, b) fifth-order stencil for computing q_L and q_R for smooth flow conditions, c) illustration of a distribution with a discontinuity, and d) adapted stencil in presence of a discontinuity.

construct one-sided high-order solutions near the grid boundaries created by a distributed grid partition. This work explores three different implementations of the numerical treatment of seventh-order ENO schemes near overset grid boundaries. The relative merits of these schemes for capturing vortex wakes arising from wings and rotor blades are summarized.

II. High-Order Methods for the Accurate Prediction of the Wake

The unsteady Reynolds averaged Navier–Stokes equations can be written as

$$\frac{\partial}{\partial t}\int_{\Omega} q\,\mathrm{d}V + \oint_S [(V_F - V_G)q + F]\,\mathrm{d}\boldsymbol{S} = \oint_S F_v\,\mathrm{d}\boldsymbol{S} \qquad \mathrm{d}\boldsymbol{S} = \left|\mathrm{d}\boldsymbol{S}\right|_n^{\mathbf{r}} \tag{1a}$$

Equation (1a) can be discretized as follows:

$$\frac{\partial}{\partial t}(q\Omega_J) + \sum_{i=1}^{6}[(V_F - V_G)q + F]_i \cdot \Delta S_i = \sum_{i=1}^{6} F_{v,i} \cdot \Delta S_i \tag{1b}$$

This formulation allows for arbitrary motion of the grids. In the current work, Eq. (1b) is solved within the structured grid, hexahedral framework. The cell-averaged solution vector q is stored at the nodes of the grid. Hexahedral cell faces are constructed virtually at the half nodes of the grid points. The temporal discretization is implemented using a three-point stencil, and the solution update process uses a Newton iterative solver to achieve third-order temporal accuracy. The viscous fluxes are computed using standard second-order central differences. The inviscid fluxes are updated using an approximate Riemann solver as described by Roe [14], that is, the numerical flux on the cell faces is given by

$$F = \frac{F_L(q_L) + F_R(q_R)}{2} - |A|(q_R - q_L) \tag{2}$$

In Eq. (2) F_L, and F_R are the left and right cell-face fluxes.

A. Fifth/Seventh-Order ENO Scheme

The fifth/seventh high-order formulation for the Navier–Stokes solution has been developed along the lines of ENO methods developed originally by Shu and Osher [6,7]. The higher order reconstruction comes in the projection stage of the conservative variable, that is, q_L and q_R.

The details of the implementation are provided elsewhere [9,10]. The formulation is briefly discussed next for completeness. The high-order reconstruction for a three-dimensional flowfield solution is broken down as three independent one-dimensional reconstructions in the three computational dimensions. Such a breakdown is feasible as the current implementation uses a structured grid framework (ξ, η, and ζ generalized grid directions) with half-node cell faces forming virtual hexahedral volumes when solving Eq. (1b), and hence is equivalent to a finite difference formulation. Breaking the three-dimensional problem into three one-dimensional problems keeps the overall computing efforts within a manageable limit, while retaining a large portion of the benefits of the high-order reconstruction. The high-order ENO reconstruction in a single dimension is described next.

For a one-dimensional initial boundary value problem, the system of hyperbolic conservation laws may be written as

$$q_t + \nabla f(q) = 0, \qquad q(x,0) = q_0(x) \tag{3}$$

The updated solution at the next time step, $n+1$, can be written as,

$$q_j^{n+1} = A(C_j)E(\tau)R(x;q^n) \tag{4}$$

Here, q is the vector cell-averaged state variables, R is the reconstruction polynomial approximation of the actual solution over the cell constructed using the available cell averages, E is the evolution operator that advances the solution by a given time step, and A is the averaging operator over cell C_j to get back the cell averages at the next time step. The high-order reconstruction can either be directly applied to the fluxes themselves or to the cell-averaged state variables before using those values to compute the fluxes. In this work, the second approach was used. The high-order construction was applied to the state variables and the approximate Riemann solver was used as the evolution operator. The fifth-order reconstruction is done as follows.

Let $J(i)$ be the vector containing the stencil index for the ith grid point and C_j denote the cell associated with node j. Given the cell averages q_j of a function $q(x)$ we need reconstruction R such that

$$R(x;q) = q(x) + O(h^r), \qquad A(C_j)R(x;q) = q_j, \qquad j \in J(i) \tag{5}$$

where r is the required order of accuracy. The polynomial R can be expressed as a Taylor expansion around the centroid of cell i.

$$R_i(x;q) = \sum_{k=0}^{r-1}\frac{1}{k!}(x - c_i)^k D_k, \qquad D_k = \frac{\partial^k q}{\partial x^k}(c_i) + O(h^{r-k}) \tag{6}$$

The D_ks may be evaluated by

$$A(C_j)R_j = q_j, \qquad j \in J(i) \tag{7}$$

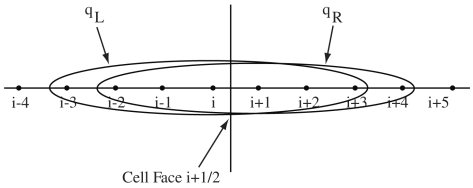

Fig. 2 Seventh-order stencil for computing q_L and q_R for smooth flow conditions.

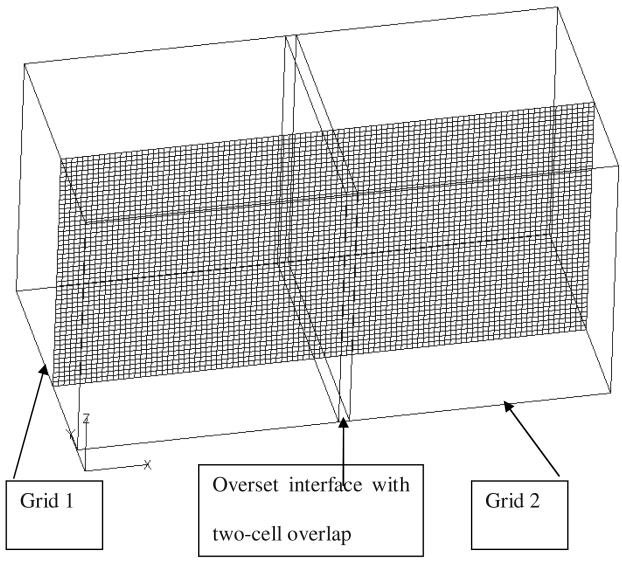

Fig. 3 Overset grids with two-cell overlap.

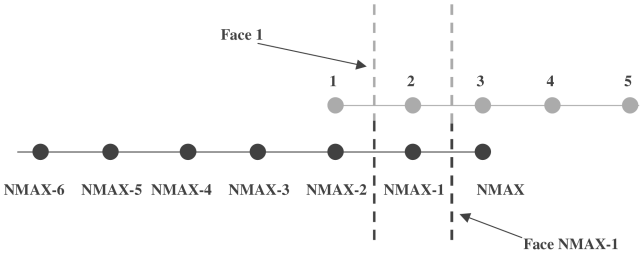

Fig. 4 Schematic of the treatment of the fluxes near the overset interface (method 1: first order near the overset interface).

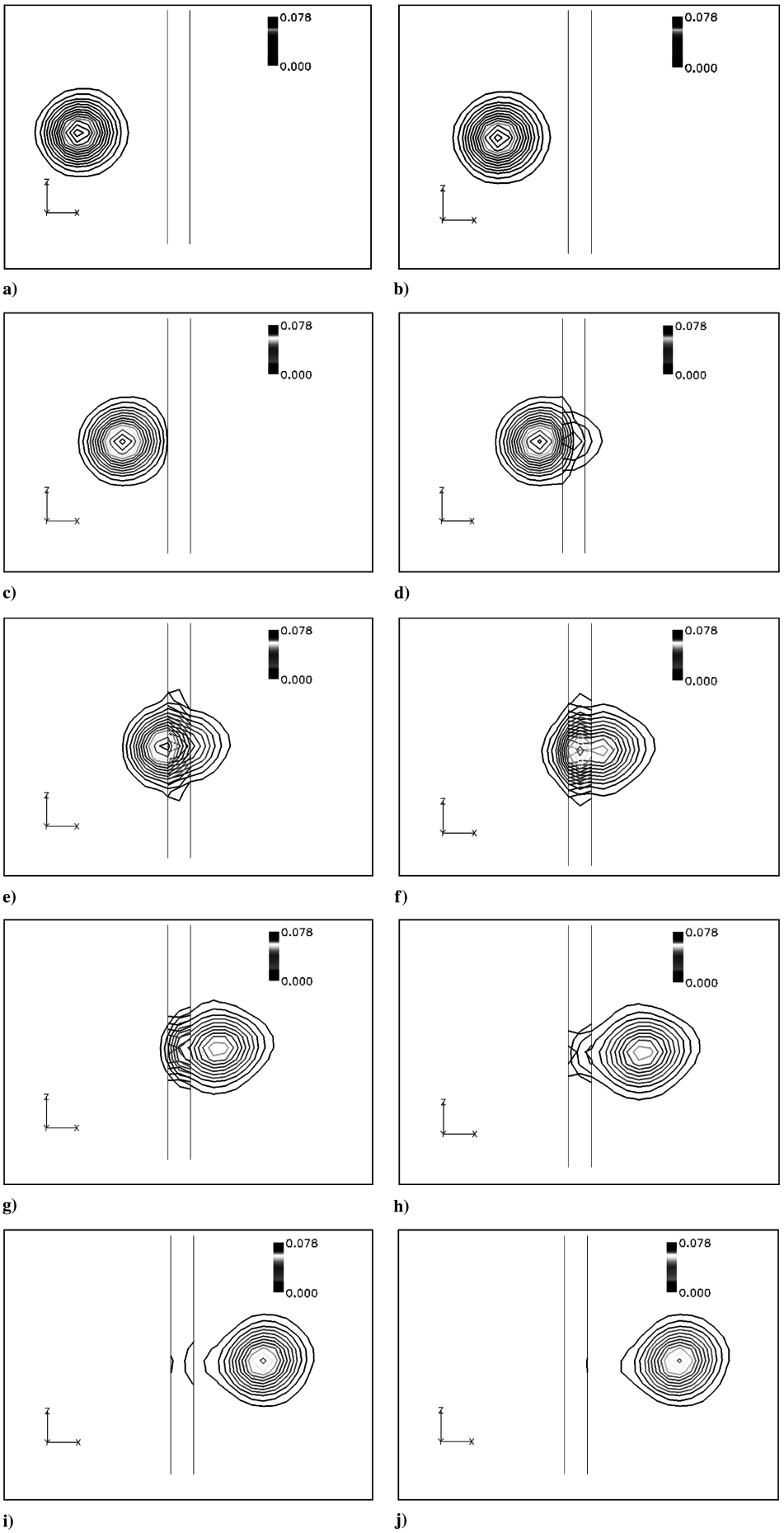

Fig. 5 Vorticity contours showing Lamb's vortex propagation across interface (method 1: first order near the overset interface).

This yields a system of equations for the D_ks:

$$\sum_{k=0}^{r-1} a_{j,k} D_k = q_j, \qquad j \in J(i)$$

$$a_{j,k} = \frac{1}{k!} A(C_j)(x - c_i)^k = \frac{1}{k!|C_j|} \int_{C_j} (x - c_i)^k \, dV \tag{8}$$

$$|C_j| = \int_{C_j} dV$$

Inverting this system, the D_ks are determined. Using these values of the D_ks, R can be constructed using Eq. (6).

An economic stencil adapting strategy is adopted in the implementation. For a fifth-order scheme, there are five possible stencil variations that will include cell i, for either q_L or q_R. The five possible stencils for q_L are shown in Fig. 1a. For a smooth flow, the most symmetric stencil (with an upwind directional bias of half a cell) is preferred. In the present implementation, the stencil to be used for each point is stored. In case of a smooth flow, the stencil pattern is set once after the flow solver is initiated. In case of an unsteady flow with shocks, the stencil adaptation is done throughout all the domains at every so many time steps (typically every 10 time steps). At every grid point, the stencil to be used is decided by comparing a weighted absolute value of the derivatives, as shown:

$$D_{\text{sum}} = \sum_{k=0}^{r-1} \alpha_k |D_k| \tag{9a}$$

The weight factors αs used in the present work were as follows:

$$\alpha_0 = \alpha_4 = 1.0 \qquad \alpha_1 = \alpha_3 = 0.8 \qquad \alpha_2 = 0.6 \tag{9b}$$

The aforementioned setting for the weight factors α_k will direct the ENO algorithm to select the centered stencil in regions where the flow properties are smooth. Such a preference will rule out wild oscillations of the stencil due to minor changes in the derivatives at every time step. This will ensure that unless discontinuities are encountered in the flowfield the centered stencil is preferred as shown in Fig. 1b. In case a discontinuity is present in the sampling region, that is, as illustrated in Fig. 1c, the sampling stencils are automatically shifted to avoid sampling across the discontinuity, as shown in Fig. 1d.

The time stepping is done in an implicit manner using directional factorization [15]. A third-order Newton iterative scheme is used to integrate in time. The use of overset grids creates internal boundary points as described by Hariharan and Sankar [15]. The information for updating these internal boundary points comes from the corresponding donor overset grid and is typically lagged by a single iteration. The subiterative scheme ensures convergence of the solution between all the overset grids in a given time step. The temporal update was done using a three-point temporal stencil, that is,

$$\frac{\partial}{\partial t}(q^{n+1}) \cong \frac{(3q^{n+1} - 4q^n + q^{n-1})}{2\Delta\tau} + O(\Delta\tau^2) \tag{10}$$

The seventh-order ENO scheme is constructed along similar lines as the fifth-order scheme already outlined. A wider stencil as shown in Fig. 2 is used for the left and right projection. The stencil shifting near the boundaries and discontinuities is similar to the fifth-order implementation.

In a three-dimensional structured grid environment, three independent one-dimensional reconstructions are done in each of ξ, η, and ζ directions. For a purely Cartesian grid, the ξ, η, and ζ coordinate directions resolve into the $\boldsymbol{i}$, $\boldsymbol{j}$, and $\boldsymbol{k}$ directions, respectively. At each grid node, the preferred ENO stencil in each of the ξ, η, and ζ directions is stored. The details of the computational costs of the fifth-order and the seventh-order ENO schemes in comparison to a standard MUSCL-based third-order scheme for a three-dimensional wing wake simulation are provided in Hariharan [16].

III. Advanced Methods for Convection of a Vortex Across an Overset Interface

ENO schemes use large stencil support for constructing progressively high-order accuracy spatial schemes. The handling of such schemes near overset boundaries influences the overall solution accuracy for large-scale computations. An ENO-based fifth/seventh-order spatially accurate Euler/Navier–Stokes overset solver was used to study the convection of vortices across overset interfaces. Different treatments of fifth/seventh schemes near overset interfaces were studied in some detail using different overset-grid configurations. In Sec. III.A, three different near-interface ENO formulations are discussed. The ability of these formulations to preserve a vortex convection across a pair of minimally overset grids is discussed. In Sec. III.B, the minimal-overlap condition for the oversetting is relaxed, and also the effect of multiple interpolation layer is discussed. In Sec. III.C, the convection across overset grids with varying grid densities is explored.

A. Minimal Overlap of Grids

Three different numerical formulations near the boundary interfaces were constructed, and their ability to preserve high-order solution accuracy near the overset interface boundaries was studied. Two overlapping Cartesian meshes were generated, and a Lamb's vortex was convected across the overset interface between the two meshes. The mesh is shown in Fig. 3. The grids consisted of 50 nodes each in the x and z directions. The grids constructed were three-dimensional employing 7 nodes in the y direction. Symmetric boundary conditions were enforced in the y direction. The Lamb's vortex was introduced with its axis aligned in the y direction. In principle, excessive oversetting causes computational inefficiency, that is, the same physical domain is computed by two different sets of

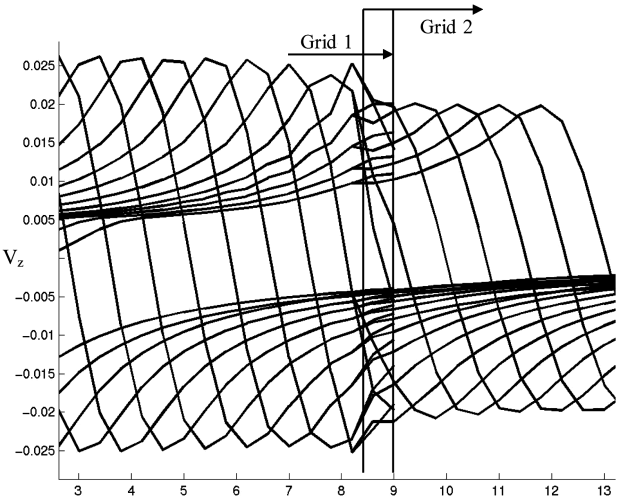

Fig. 6 Tangential velocity distribution across the vortex as it convects through the interface (method 1: first order near the overset interface).

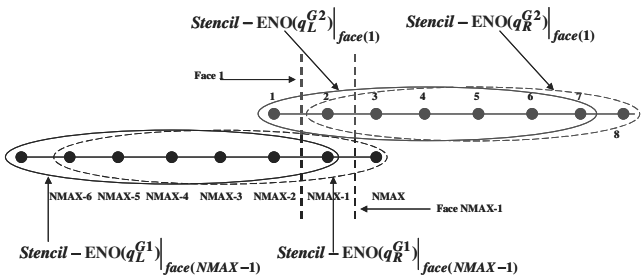

Fig. 7 Schematic of the treatment of the fluxes near the overset interface (method 2: uniformly seventh-order ENO computation over the entire domain using one-sided stencils near boundaries).

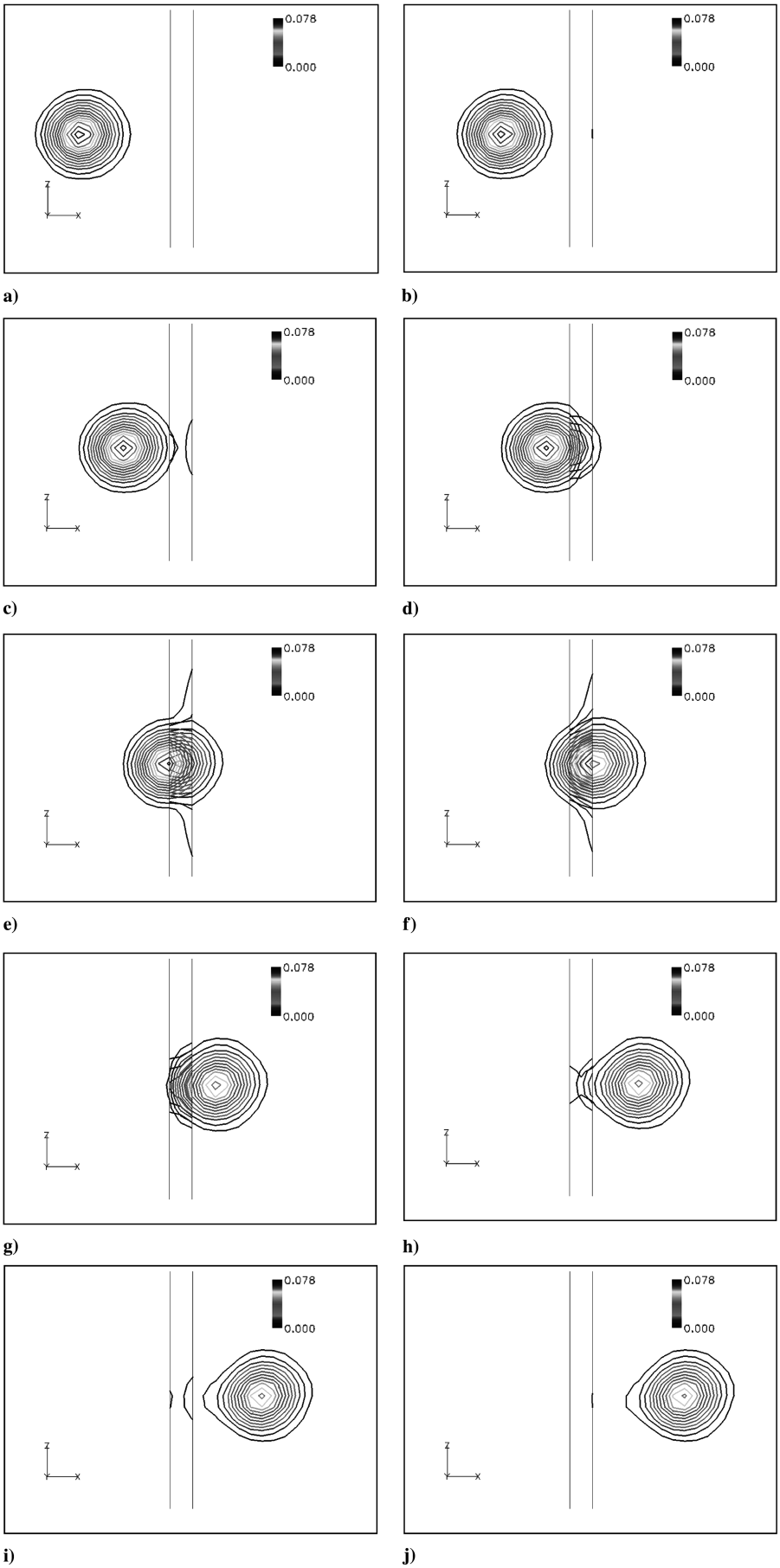

Fig. 8 Vorticity contours showing Lamb's vortex propagation across interface (method 2: uniformly seventh-order ENO computation over the entire domain using one-sided stencils near boundaries).

grid points, and one would like to minimize such overlaps. This is especially true for large-scale rotor flow computations wherein oversetting is used as a means of grid break up or as a method of refinement for parallel computations. From the standpoint of the preservation of a vortex transferring across overset interfaces, the minimal interface poses the most stringent requirements for noncompact high-order schemes, as such schemes require a wide-stencil support.

Three different implementations of the fluxes near the overset boundaries for grid 1 (G1) and grid 2 (G2) were considered. Figure 4 shows a one-dimensional schematic of the first implementation (method 1). In this case, the boundary points of G1 were interpolated from G2 and vice versa. The computational order of spatial accuracy near the boundary cell was dropped to first order, that is

$$q^{G1}_{NMAX} = q^{G2}_{3} \qquad q^{G2}_{1} = q^{G1}_{NMAX-2} \qquad q^{G1}_{R,NMAX-1} = q^{G1}_{NMAX}$$
$$q^{G1}_{L,NMAX-1} = q^{G1}_{NMAX-1} \qquad q^{G2}_{R,1} = q^{G2}_{2} \qquad q^{G2}_{L,1} = q^{G2}_{1} \tag{11}$$

The Lamb's vortex was initiated in the center of G1. Figures 5a–5j show a sequence of images showing the vortex as it convects down and across the overset interface. The vortex is well within G1 in Figs. 5a and 5b and is seen to be in full strength without any distortions. As it approaches the interface (Fig. 5c), the vortex starts to distort. The vortex begins to transfer to G2 in Fig. 5d and is clearly seen to appear in G2 in a dissipated form. The contour plots in the overlap region consist of the vorticity in G1 and G2 as well. If the vortex is transferred perfectly, the contours should be identical. Figures 5e–5h capture the process of the vortex crossing over the interface. The vortex has completely transferred over to G2 in Figs. 5i and 5j. The use of method 1 boundary treatment results in a significant loss of resolution of the vortex during the transfer process.

Figure 6 shows the plots of tangential velocity variation across the vortex at several instances in the process of the vortex crossover. A single crossover results in the reduction of the peak-to-peak strength of the vortex by approximately 40%. The use of method 1 would largely negate any advantages of the current high-order scheme if multiple overset grids were used.

To improve the accuracy near the interface, method 2 was developed. Figure 7 shows a schematic illustrating method 2. In method 2, the adaptive nature of the stencils in an ENO scheme is used to construct a seventh-order accurate solution all the way to the overset interface. This is achieved by shifting to one-sided stencils near the boundaries. In Fig. 7, the two stencils employed to compute q_L and q_R for faces (NMAX-1, G1) and (1, G2) are shown. The left and right stencils are staggered by a one cell difference. The treatment of the fluxes near the overset interface can be summarized as

$$q^{G1}_{NMAX} = q^{G2}_{3} \qquad q^{G2}_{1} = q^{G1}_{NMAX-2} \tag{12a}$$

for the grid points (NMAX, G1) and (1,G2), and

$$q^{G1}_{R,NMAX-1} = \mathrm{ENO}\left(q^{G1}_{R,NMAX-1}\right) \qquad q^{G1}_{L,NMAX-1} = \mathrm{ENO}\left(q^{G1}_{L,NMAX-1}\right)$$
$$q^{G2}_{R,1} = \mathrm{ENO}\left(q^{G2}_{R,1}\right) \qquad q^{G2}_{L,1} = \mathrm{ENO}\left(q^{G2}_{L,1}\right) \tag{12b}$$

for the primitive variables at the cell faces (NMAX-1, G1) and (1, G2). In Eq. (12b), the ENO(·) operator stands for the projection using the seventh-order ENO method.

Figures 8a–8j show a sequence of images for computations using method 2, similar to Fig. 5, showing a vortex as it convects down and across the overset interface. The vortex is well within G1 in Figs. 8a and 8b and is seen to be in full strength without any distortions. The vortex approaches the interface (Fig. 8c) without dissipation/distortion. The vortex begins to transfer to G2 in Fig. 8d and, as can be seen in images 8d–8f, the vortex transfers in an intact form without excessive dissipation. The vortex has completely transferred over to G2 in Figs. 8i and 8j, at which point it has dissipated to some extent when compared with the original vortex in G1.

Figure 9 shows the plots of tangential velocity variation across the vortex at several instances in the process of the vortex crossover for method 2. A single crossover results in the reduction of the peak-to-peak strength of the vortex by approximately 10%. The use of method 2 would still result in a significant loss of vortex strength if several overset grids were used in a computation. For accurately capturing phenomena such as BVI noise, the tip vortex from a rotor blade has to be captured without dissipation for over 3–4 blade revolutions. A typical distributed, overset-grid computation would involve several overset interface information transfers before the tip vortex travels such distances.

Method 3 was developed to further improve the accuracy of the computation near the interfaces, and it leverages the ENO projection of face fluxes. Figure 10 shows a schematic illustrating method 3. First, as in method 2, one-sided stencils are used near the interface boundaries. Further, the primitive variables at the two cell faces near the interface boundary (NMAX-1,G1) and (1,G2) are directly interpolated from each other. The interface treatment can be summarized as

$$q^{G1}_{NMAX} = q^{G2}_{3} \qquad q^{G2}_{1} = q^{G1}_{NMAX-2} \tag{13a}$$

for the grid points (NMAX, G1) and (1,G2), and

$$q^{G1}_{R,NMAX-1} = \mathrm{ENO}\left(q^{G2}_{R,2}\right) \qquad q^{G1}_{L,NMAX-1} = \mathrm{ENO}\left(q^{G2}_{L,2}\right)$$
$$q^{G2}_{R,1} = \mathrm{ENO}\left(q^{G1}_{R,NMAX-2}\right) \qquad q^{G2}_{L,1} = \mathrm{ENO}\left(q^{G1}_{L,NMAX-2}\right) \tag{13b}$$

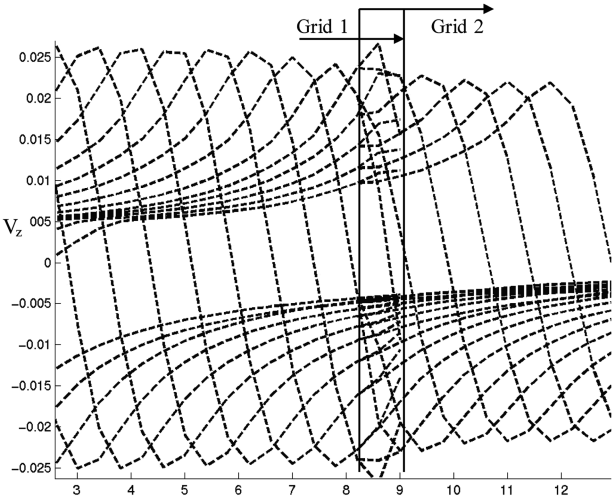

Fig. 9 Tangential velocity across the vortex as it convects through the interface (method 2: uniformly seventh-order ENO computation over the entire domain using one-sided stencils near boundaries).

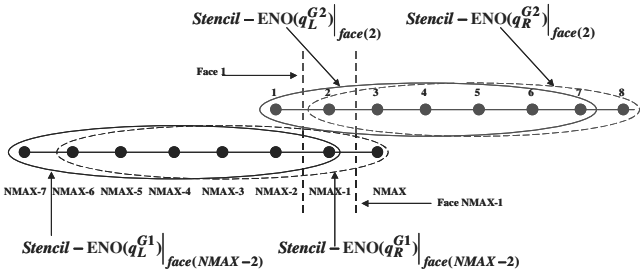

Fig. 10 Schematic of the treatment of the fluxes near the overset interface (method 3: uniformly seventh-order ENO computation over the entire domain using one-sided stencils near boundaries and flux projection on overset cell faces).

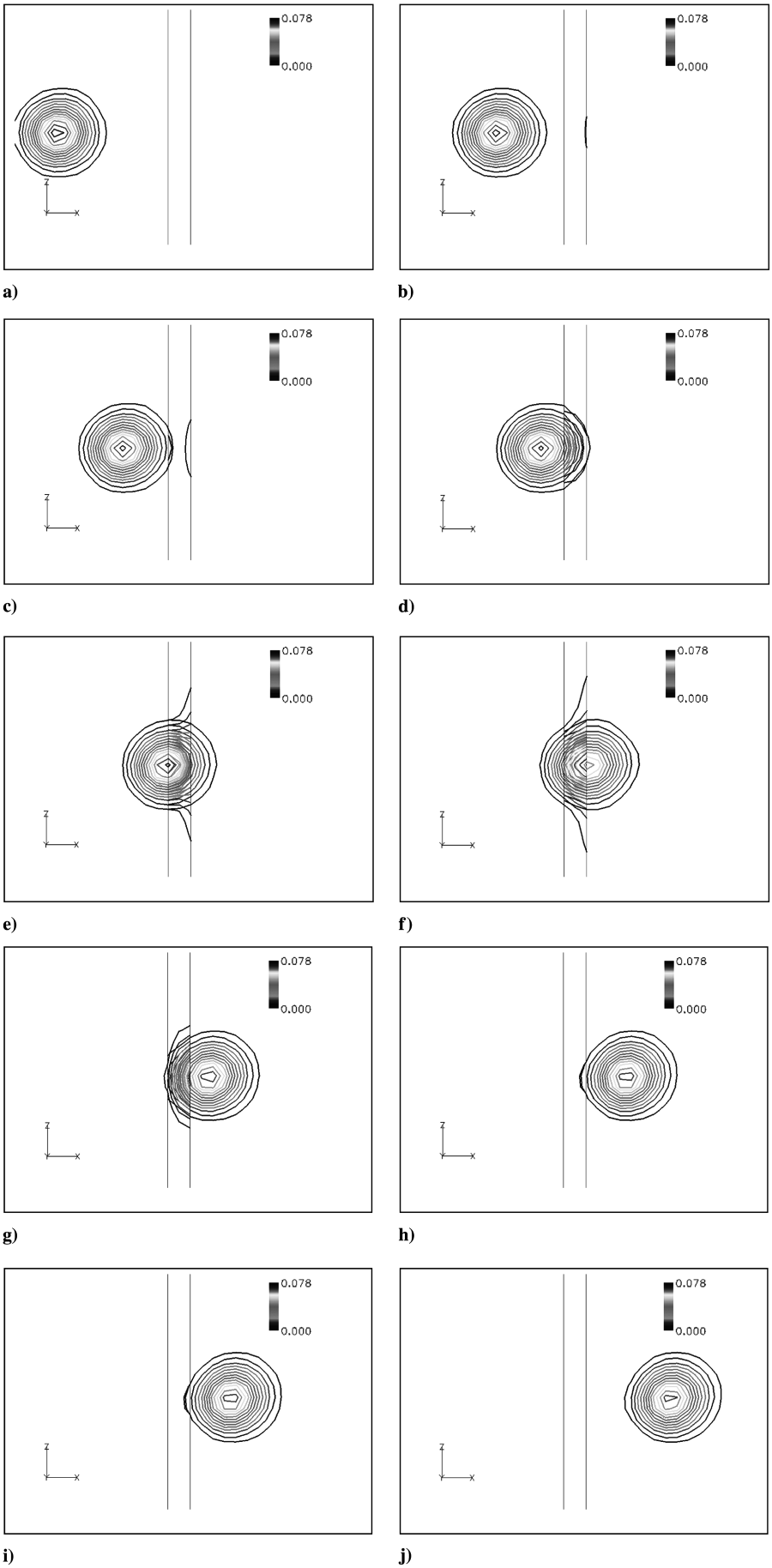

Fig. 11 Vorticity contours showing Lamb's vortex propagation across interface (method 3: uniformly seventh-order ENO computation over the entire domain using one-sided stencils near boundaries and flux projection on overset cell faces).

for the primitive variables at the cell faces (NMAX-1, G1) and (1, G2).

Figures 11a–11j show a sequence of images for computations using method 3, similar to Figs. 5 and 8. The vortex contours in G1 and G2 appear almost identical as the vortex straddles the grid interface. The vortex appears in G2 (Fig. 8j) intact with no noticeable dissipation. Figure 12 shows the plots of tangential velocity variation across the vortex at several instances in the process of the vortex crossover for method 3. The peak-to-peak strength of the vortex is retained as the vortex crosses the grid interface. The use of method 3 would be desirable to retain all the advantages of a high-order scheme if several overset grids were used in a computation. Figure 13 compares all the vortex strengths as computed by the three methods in a single plot.

B. Excess Overlap of Grids

In the previous subsection, different treatments of higher order boundaries were considered for the minimal-overlap concept. Minimal overlap is desirable from the standpoint of computational efficiency and becomes vital if a large grid is distributed among a number of processors. For example, a background Cartesian grid to compute rotor in hover, consisting of 25 million grid points, may be broken up into 25 distributed pieces. In such a case, having excessive overlap in all three directions will result in a substantial number of grid points covering the same region of space.

However, there may be other instances in which the two-cell overlap may be excessively restrictive. For example, when an O-type grid is placed in a background grid, the "fringe point" overset boundaries of the background grid are usually set at least five–six points within the O-grid far-field boundaries. A schematic of a typical oversetting of an O-type blade grid with a background grid is shown in Fig. 14a. The presence of an overset body grid will generate internal boundary points (fringe points) in the background grid that interpolate information from the blade grid. The hole in the background grid is usually cut such that the fringe points are well

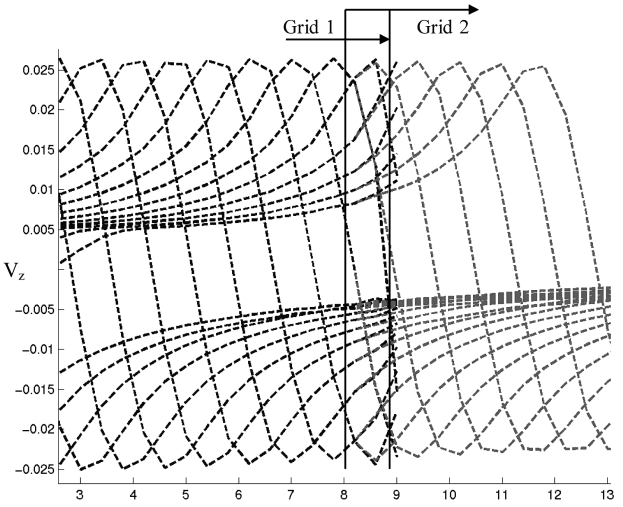

Fig. 12 Tangential velocity across the vortex as it convects through the interface (method 3: uniformly seventh-order ENO computation over the entire domain using one-sided stencils near boundaries and chimera flux interpolation).

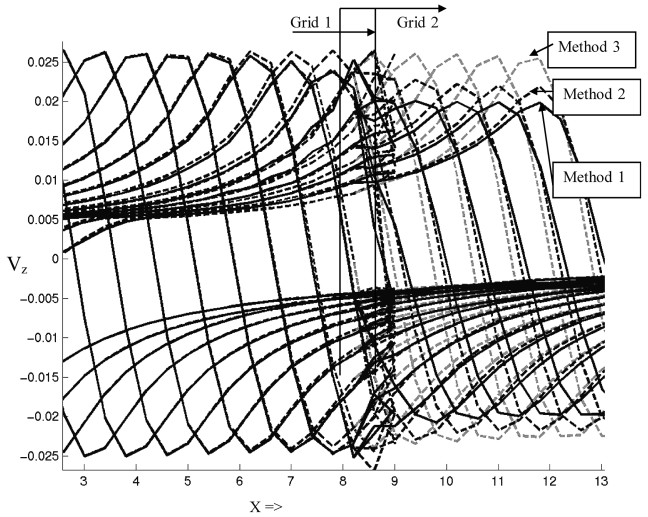

Fig. 13 Tangential velocity across the vortex as it convects through the interface. Comparison of results from methods 1, 2, and 3.

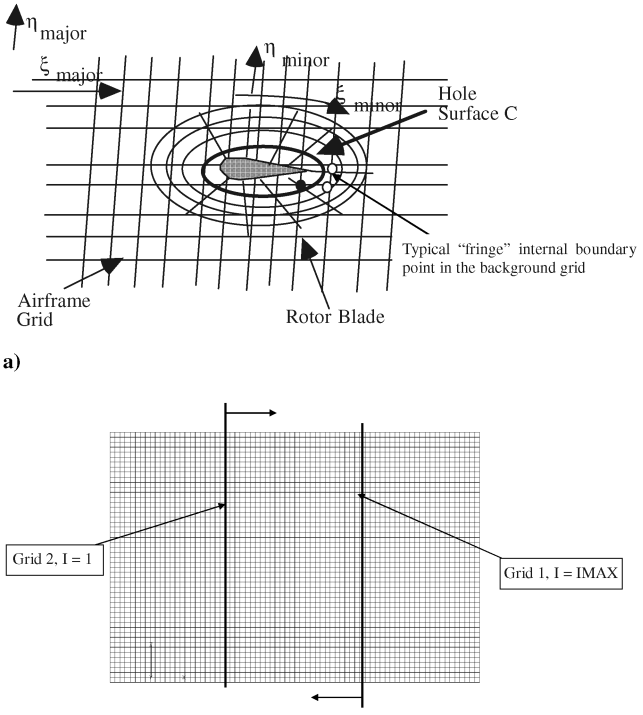

Fig. 14 Overset grids with excess overlap: a) Schematic of a blade grid (O type) overset with a background grid (Cartesian) in a typical rotorcraft configuration. Internal boundary points in the background grid due to holes cut by the blade are well inside the blade grid. b) Grid system for overset transfer with excess overlap.

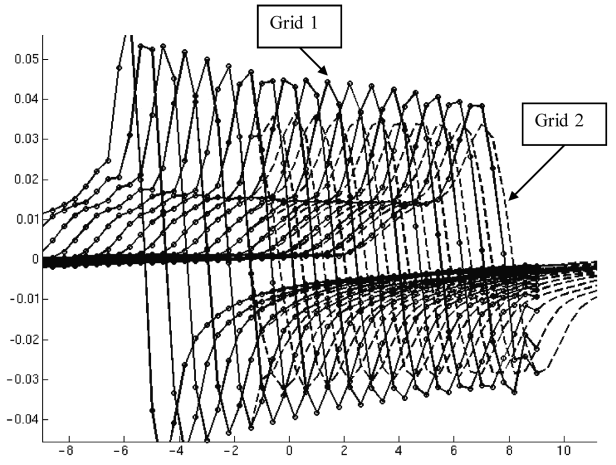

Fig. 15 Tangential velocity across the vortex as it convects through the extended interface (method 1: uniformly seventh-order ENO computation, first order near the boundaries; four points across initial core).

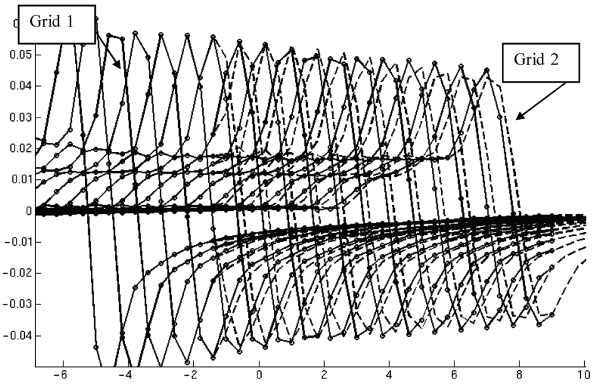

Fig. 16 Tangential velocity across the vortex as it convects through the extended interface (method 2: uniformly seventh-order ENO computation over the entire domain, one-sided stencils near the boundaries; four points across initial core).

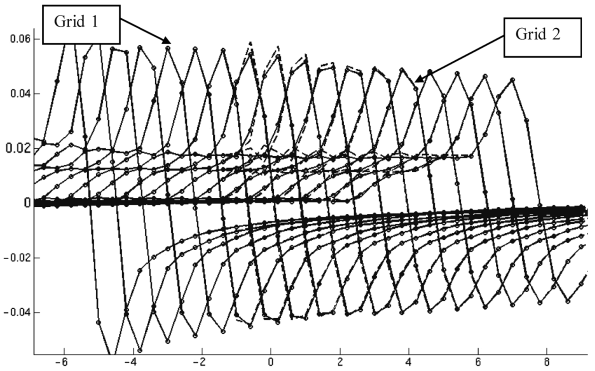

Fig. 17 Tangential velocity across the vortex as it convects through the extended interface (method 3: uniformly seventh-order ENO computation over the entire domain using one-sided stencils near boundaries and chimera flux interpolation; four points across initial core).

inside the blade grid region. Such overset fringe boundary points associated with blade (or, in general, body) grids are limited in typical rotorcraft wake computations in comparison with overset boundary points generated due to the break up of a large background Cartesian mesh for distributed computing purposes, and hence one can tolerate some computational inefficiency.

In this subsection, we investigate the three methods outlined in Sec. III.A when the minimal-overlap condition is relaxed. Figure 14b shows a Cartesian grid system consisting of two grids with an overlap

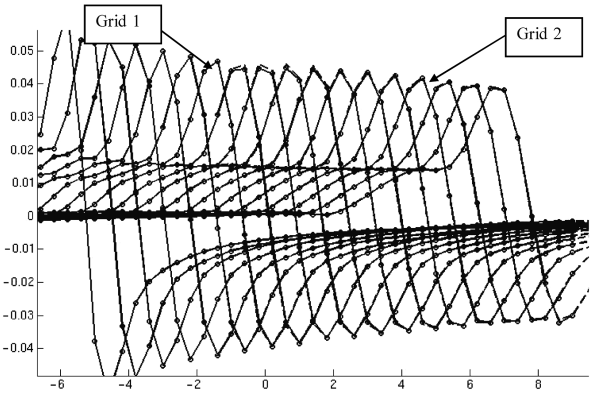

Fig. 18 Tangential velocity across the vortex as it convects through the extended interface (method 3: uniformly fifth-order ENO computation over the entire domain using one-sided stencils near boundaries and chimera flux interpolation; four points across initial core).

region of 25 grid cells. In this study, the initial core size of the vortex was varied from 4 to 10 cells across the peak-to-peak variation. Therefore, even for the well-resolved case of 10 cells across the vortex core, the vortex will always be well within either one of the grids at all times as it convects across. The variation in core size was done to arrive at the minimal grid requirement metrics in the Cartesian settings.

Figure 15 shows a carpet plot of the tangential velocity variation for the seventh-order ENO solution across the vortex at various streamwise locations as the vortex moves across. The boundary treatment outlined in method 1 was applied at the interfaces. The plots span grid 1 (solid) and grid 2 (dashed). The grid point locations are also identified for the grid 1 plots to ascertain the number of grid points between the peak-to-peak tangential velocity variation. The vortex was initialized in grid 1, as before, but with four grid points across the vortex core. Two issues are of interest. The first is the diffusion not related to boundary treatment effects. Even within grid 1, the peak-to-peak variation decays as the seventh-order scheme cannot hold the initial prescribed vortex at four points across the core without diffusion. The number of grid points across the core tends to settle down at five–six points across the core, as seen from the downstream stations. The second issue is the decay at the intergrid boundary if method 1 is applied. As one would expect, guided by results in the earlier subsection, there is more than 30% decay of the peak-to-peak core velocity as the vortex transfers to grid 2. This result was similar to the minimal-overlap case using method 1 discussed in the last subsection. Using the first-order boundary treatment will be equally detrimental irrespective of minimal or excessive grid overlap.

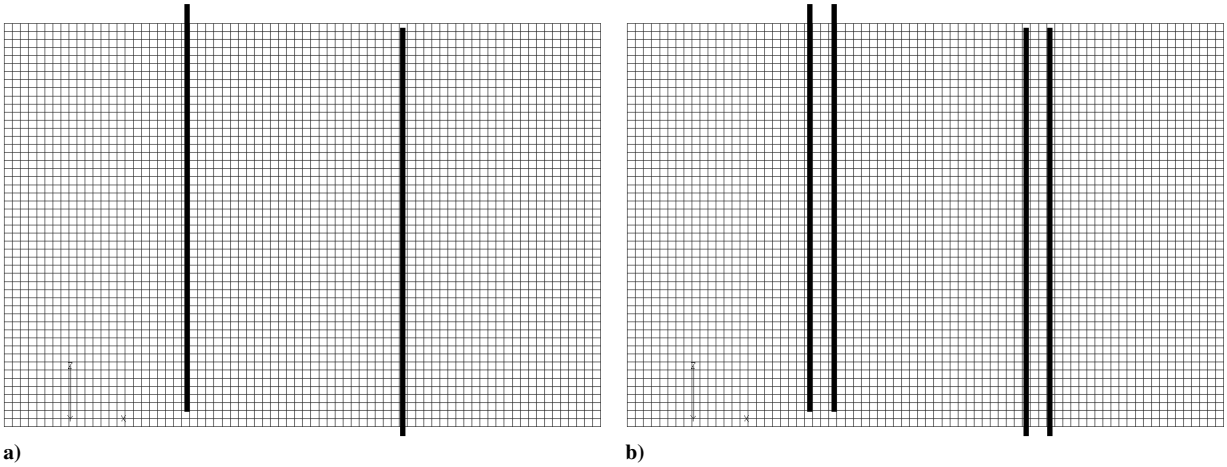

a) b)

Fig. 19 Multiple-layer interpolation: a) single, and b) double layer of overset interpolation.

Figure 16 shows a similar plot using method 2. The initial core size was still maintained at four grid points across, and hence the overall peak-to-peak decay to fit at five–six grid points across the vortex was similar. However, at the interface the peak-to-peak variation was captured in grid 2 with no noticeable dissipation, but with a small shift in the vortex location. Compared with the minimal-overlap case, the vortex is transferred across to grid 2 with higher fidelity. This is to be expected as only one grid uses one-sided stencils near the boundary interface when there is excess grid overlap. The shift in the location of the vortex center was less than 5% of the vortex core size. However, even such a small shift may affect computations that require an accurate vortex position, that is, rotor blade in hover wherein the location of the first-passage vortex plays a large part in accurately determining the tip loads.

Figure 17 shows a similar plot when method 3 is used. At the interface, the vortex is transferred to grid 2 with no noticeable difference in the core structure. Irrespective of whether the oversetting is minimal or excessive, method 3 produces the cleanest transfer. However, for the excess-overlap case, method 2 introduces only small discrepancies in the transferred vortex strength and location. Figure 18 shows the result when the fifth-order scheme is used instead of the seventh. The overall dissipation associated with the fifth order is higher (the vortex will settle down eventually at approximately 10 points across the core), but the interface transfer characteristics are similar to the seventh-order result in Fig. 17.

In the excess-overlap settings, an alternative to directly interpolating the fluxes as in method 3 is to interpolate multiple layers of internal boundary points. Figure 19b illustrates this concept for two layers of interface interpolation (usually referred to in the overset literature as “double layer”). The first two streamwise layers of grid 2 and the last two streamwise layers of grid 1 derive their flow information from grid 1 and grid 2, respectively. Figure 19a shows the standard single-layer concept for comparison. For obvious reasons, one cannot implement double-layer interpolation when the overlap region is two or three cells.

Because the earlier studies in this section established that the seventh-order scheme required five–six grid points across the core to avoid dissipation, the vortex was reinitialized with six grid points across the core. For all of the studies examining the effect of the single versus double interpolation layer, method 2 was solely used at the interface. Figure 20 shows the familiar carpet plot of the tangential velocity variation at several locations across the vortex path when single-layer interpolation is used. The vortex is seen to be transferred across the interface with no noticeable dissipation, but with a small shift in vortex position. Figure 21 shows similar results for double-layer interpolation. In this case, the vortex computed on the two grids lie right on top of each other. Using three layers of interpolation does not offer any further benefits, as seen in Fig. 22. This study shows that, wherein excess overlap is possible, method 2 with double-layer interpolation is sufficient.

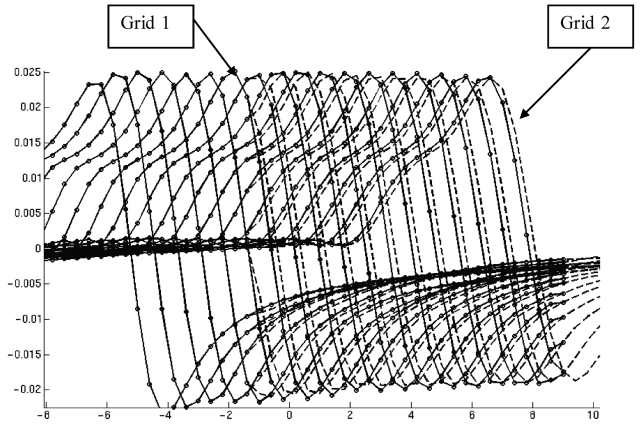

Fig. 20 Tangential velocity across the vortex as it convects through the extended interface (method 2: seventh-order ENO computation over the entire domain using one-sided stencils near boundaries and single-layer interpolation; six grid points across initial vortex core).

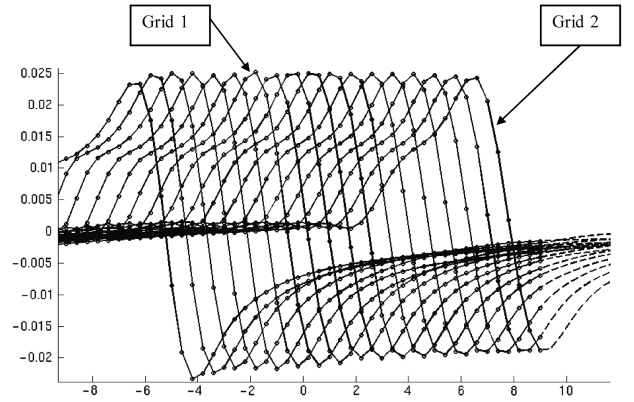

Fig. 21 Tangential velocity across the vortex as it convects through the extended interface (method 2: seventh-order ENO computation over the entire domain using one-sided stencils near boundaries and double-layer interpolation; six points across initial vortex core).

C. Overset Grids with Resolution Mismatch

So far, we have only considered vortex transfer between grids that are identical in resolution. Often in practice enforcing such a criteria may not be possible and there may be some mismatch. In this subsection, we look at some bounds on how much the resolution between two overset grids can be different without introducing any

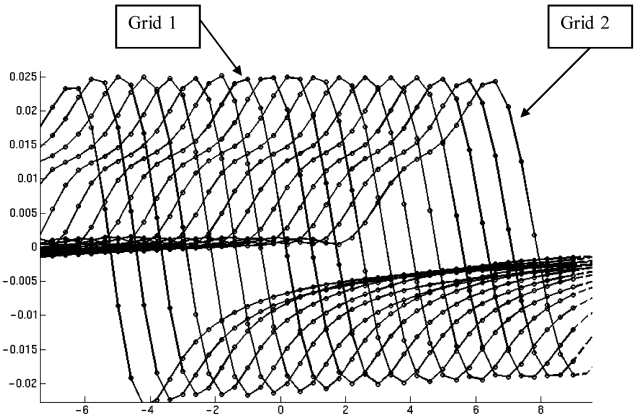

Fig. 22 Tangential velocity across the vortex as it convects through the extended interface (method 2: seventh-order ENO computation over the entire domain using one-sided stencils near boundaries and triple-layer interpolation; six points across initial vortex core).

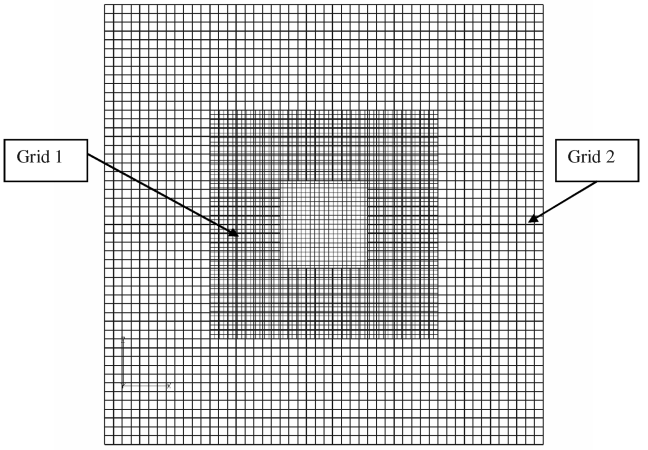

Fig. 23 Overset grids with a 2:1 grid resolution. The finer grid is entirely inside the coarse grid. The vortex is transferred to the coarser grids through internal boundary points (fringe points).

significant distortion in the strength and position of the transferred vortex.

Figure 23 shows the grid system for this study. Grid 1 has twice as much resolution as grid 2 and is immersed entirely inside grid 2. The vortex was initialized inside grid 1. The transfer to grid 2 occurred through internal boundary points generated by cutting a hole in grid 2. Such points are generally referred to as fringe points. Once again, for this study, method 2 was solely used at the overset fringe interface points. Figure 24a shows a sequence of vorticity contour plots in grid 1 as the initialized vortex transports across to the streamwise end of grid 1. Figure 24b shows similar vorticity contour plots in grid 2 as the vortex transfers across from grid 1 through the fringe points and transports across grid 2. Periodic boundary conditions had been implemented at the streamwise boundaries for grid 2, and hence the vortex feeds back into the upstream location (as seen in Fig. 24b).

The vortex was first initialized in grid 1 such that it is well resolved in both grid 1 and grid 2 when the seventh-order scheme is used, that is, nine grid points in grid 1 across the vortex core. Figure 25 shows the comparison of tangential velocity variation across the vortex at a location identified as station A in Fig. 24a. Station A is a streamwise location inside the common overlap region of grid 1 and grid 2, that is, between the fringe boundary of grid 2 and downstream boundary of grid 1. As can be seen in Fig. 25, the transferred vortex in grid 2 has no noticeable loss in strength. This can be explained if one looks at the relative grid resolutions of the two grids in comparison with what is required by the seventh-order scheme to preserve the vortex without any loss. The seventh-order scheme requires five–six grid points across the vortex core to transport without any noticeable loss in vortex strength. In this case, the vortex was initialized at nine grid points on grid 1, which is more than necessary for the seventh-order scheme. Grid 2 is half the resolution of grid 1 and would have a resolution of five grid points $[(9+1)/2]$ across the core. For the seventh-order scheme, this is just sufficient, and hence there is no noticeable loss in peak-to-peak strength in the transferred vortex.

Next, the vortex was reinitialized with seven grid points across the core in grid 1 and the aforementioned study was repeated. Figure 26 shows a similar comparison of the vortex strengths at station A. In this case, grid 2 has a resolution of four grid points across the core, which is less than what is required by the seventh-order scheme. One would expect some degradation of the transferred vortex, which indeed is the case. The peak-to-peak strength of the vortex in grid 2 is about 85% the strength in grid 1 at station A. This study was further repeated with five grid points (just resolved) across the vortex core in grid 1, which puts it at three grid points (underresolved) across the core in grid 2. Figure 27 shows the similar comparison of the vortex strengths in grid 1 and grid 2; the transferred vortex can be seen to be captured at ~50% peak-to-peak strength of the original vortex. Thus,

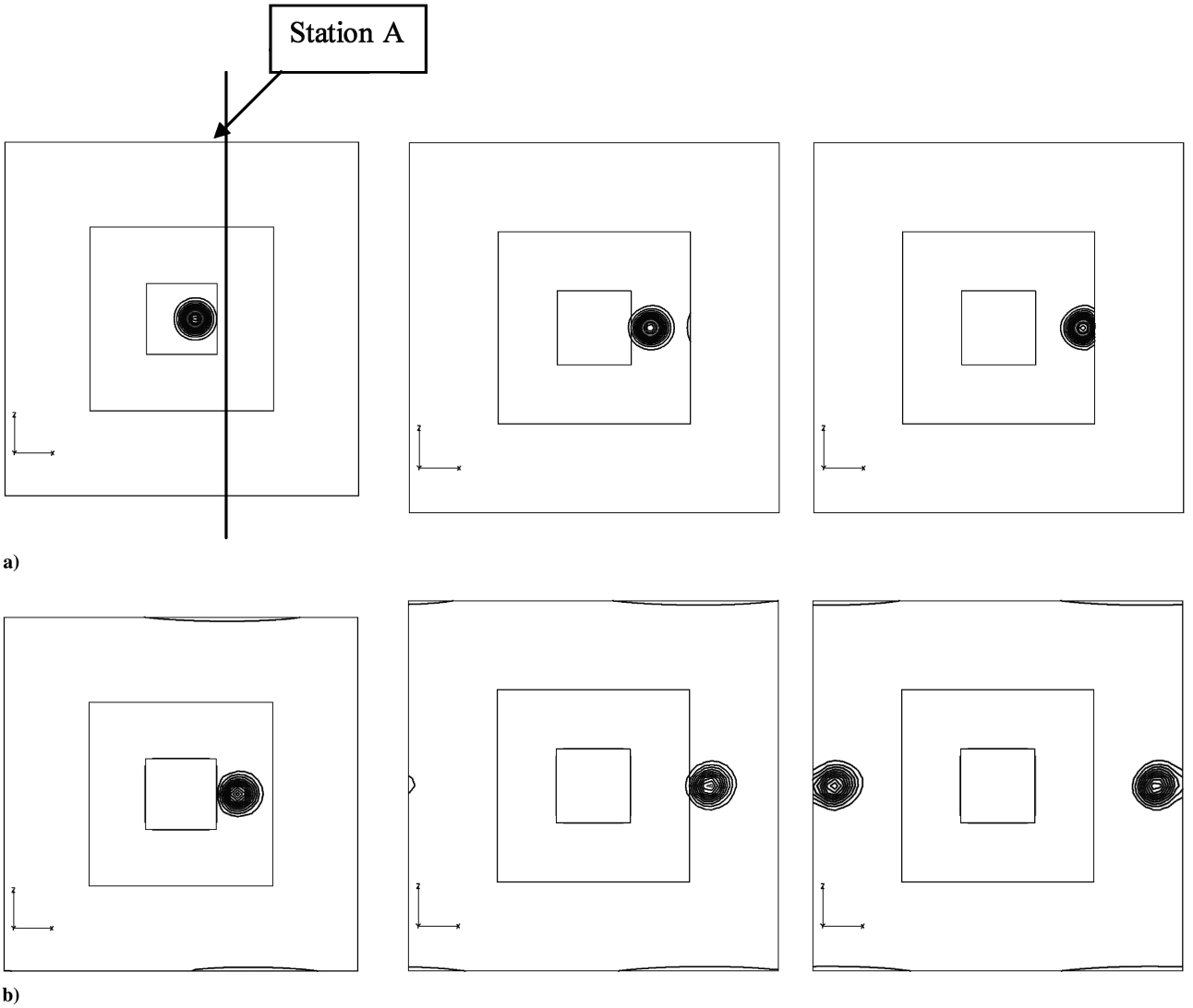

Fig. 24 Vortex transfer across resolution mismatched grids: a) vorticity contours plotted on grid 1 (method 2: seventh-order ENO computation over the entire domain using one-sided stencils near boundaries, and single-layer interpolation), and b) vorticity contours plotted on grid 2 (method 2: seventh-order ENO computation over the entire domain using one-sided stencils near boundaries and single-layer interpolation).

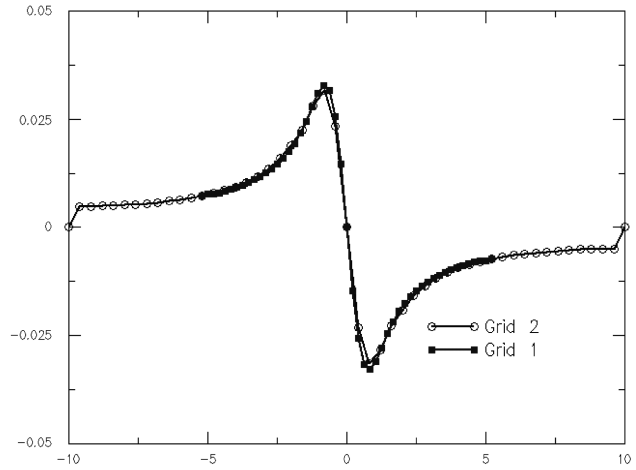

Fig. 25 Tangential velocity across the vortex at station A shown in Fig. 24a (method 2: seventh-order ENO computation over the entire domain using one-sided stencils near boundaries and single-layer interpolation; nine grid points across the vortex core in grid 1 and five grid points in grid 2).

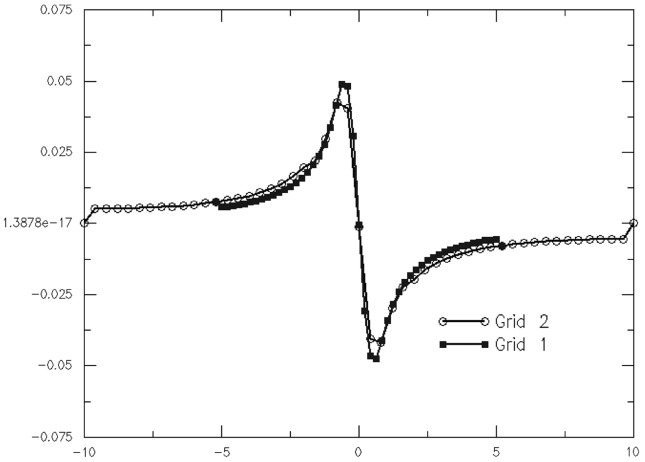

Fig. 26 Tangential velocity across the vortex at station A shown in Fig. 24a (method 2: seventh-order ENO computation over the entire domain using one-sided stencils near boundaries; seven grid points across the vortex core in grid 1 and four grid points in grid 2).

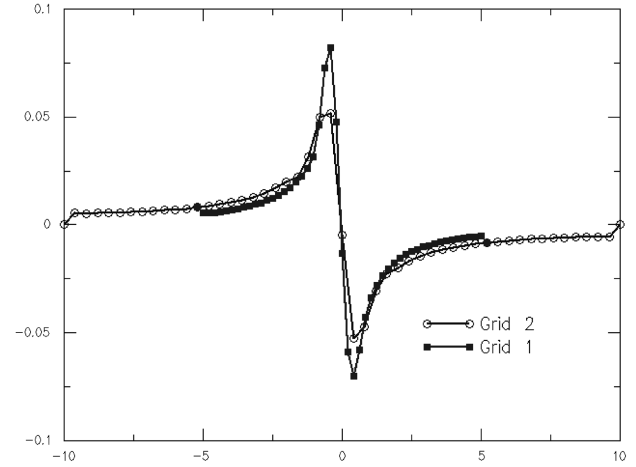

Fig. 27 Tangential velocity across the vortex at station A shown in Fig. 24a (method 2: seventh-order ENO computation over the entire domain using one-sided stencils near boundaries and single-layer interpolation; five grid points across the vortex core in grid 1 and three grid points in grid 2).

if the grids are mismatched, as long as both of the grids satisfy the minimum grid point requirements for the scheme being used, no noticeable degradation occurs in the transferred vortex. It must be noted that for the Lamb's vortex that was considered in this study the dominant gradient exists only along the tangential direction. However, for realistic three-dimensional vortices coming off a wing or a rotor, often a strong axial velocity component exists within the vortical structures. For such vortices, the grid resolution requirements should ensure that the axial gradients, which are stronger than the tangential gradients, are captured. If that is not the case, the axial velocity components will be diffused out and the vortex itself will diffuse to maintain angular momentum conservation. This effect is illustrated in a numerical study of tip vortex evolution off an NACA0015 wing by Hariharan [16].

IV. Conclusions

In this paper, the advantages of careful treatment of overset boundaries for ENO-based high-order methods in capturing vorticity were outlined. One of the drawbacks with ENO schemes is that they are not compact, and hence a wide stencil of information is required to construct the high-fidelity solution. This becomes a problem when large-scale simulations are broken into parts and distributed over a computing network, making it necessary to have sufficient overlap between the grid parts to construct a uniformly high-order accurate solution. One possible solution is to let the adaptive underlying methodology of ENO construct one-sided high-order solutions near the grid boundaries created due to a distributed grid partition. A seventh-order near-boundary ENO-scheme treatment, using such one-sided stencils and direct primitive variable interpolation, has been demonstrated to capture vortices convecting across overset interfaces with no noticeable dissipation in Cartesian grid settings. The seventh-order ENO scheme requires approximately six grid points across the vortex core to preserve the vortex. Key conclusions from the current study are as follows:

1) Maintaining a uniformly high spatial order of accuracy across overset interfaces is essential to maintaining the fidelity (strength, position) of vortex structures that transfer from one grid to another. For a fifth/seventh ENO computation, if the spatial accuracy is dropped to first order near the interface (method 1), a vortex loses $\sim$30% its peak-to-peak strength in a single transfer, irrespective of whether the overlap region is minimal or excessive.

2) Overset computations intrinsically have a duplication of computational points covering the same region in space. It is desirable to minimize the extent of the overlap to maximize computational efficiency. The ideal overlap scenario for a Cartesian grid is a single-cell overlap. Under such a scenario, a method that uses one-sided stencils near the boundaries and also directly interpolates fluxes (method 3) preserves any vortex crossing the overset interface. The peak-to-peak strength of the vortex remains undiminished and no shift errors are introduced in the vortex-center location as the vortex transfers from one grid to another.

3) If it is not required to enforce a minimal oversetting limitation, method 2 (high order near boundaries using one-sided interpolation) will be sufficient in most instances in which small vortex-center shift errors can be tolerated. If such vortex-center shift errors cannot be ignored, method 3 needs to be used. If a dual interpolation layer is used, vortex-center shift errors occurring in method 2 are eliminated.

4) If the two overset grids involved in a vortex transfer have differing grid resolutions, the primary drivers for a clean transfer are as follows: a) each grid should have enough grid resolution to capture the vortex accurately for the given level of spatial accuracy of the scheme used to compute the solution, and b) method 2 or method 3 should be used at the interface.

The high-order ENO schemes for overset interfaces described in this paper are good candidate schemes for computing rotor-blade wakes using overset background grids. They are particularly suitable for distributed large-scale overset computations, such as helicopter hover wake capturing and forward-flight blade-vortex interaction noise. Further research is needed to generalize the ENO high-order interface methods for non-Cartesian grids.

References

[1] Srinivasan, G. R., and Ahmad, J. U., "Navier–Stokes Simulation of Rotor-Body Flowfield in Hover Using Overset Grids," Confederation of European Aerospace Societies Paper C15, Sept. 1993.

[2] Strawn, R. C., and Barth, T. J., "Unstructured Adaptive Mesh Computations of Rotorcraft High-Speed Impulsive Noise," *Journal of Aircraft*, Vol. 32, No. 4, 1996, pp. 754–760.

[3] Duque, E. P. N., and Srinivasan, G. R., "Numerical Simulation of a Hovering Rotor Using Embedded Grids," *48th Annual AHS Forum*, American Helicopter Society, Alexandria, VA, May 1992, pp. 429–445.

[4] Duque, E. P., "A Structured/Unstructured Embedded Grid Solver for Helicopter Rotor Flows," *50th Annual AHS Forum*, American Helicopter Society, Alexandria, VA, May 1994, pp. 1249–1258.

[5] McCroskey, W. J., "Wake Vortex System of Helicopters," AIAA Paper 95-0530, Jan. 1995.

[6] Shu, C.-W., and Osher, S., "Efficient Implementation of Essentially Non-Oscillatory Shock-Capturing Schemes 1," *Journal of Computational Physics*, Vol. 77, No. 2, 1988, pp. 439–471. doi:10.1016/0021-9991(88)90177-5

[7] Shu, C.-W., and Osher, S., "Efficient Implementation of Essentially Non-Oscillatory Shock-Capturing Schemes 2," *Journal of Computational Physics*, Vol. 83, No. 1, 1989, pp. 32–78. doi:10.1016/0021-9991(89)90222-2

[8] Harten, A., Engquist, B., Osher, S., and Chakravarthy, C. R., "Uniformly High Order Accurate Essentially Non-Oscillatory Schemes 3," *Journal of Computational Physics*, Vol. 131, No. 1, Feb. 1997, pp. 3–47. doi:10.1006/jcph.1996.5632

[9] Hariharan, N., and Sankar, L. N., "Higher Order Numerical Simulation of Rotor Flow Field," *AHS Forum and Technology Display*, American Helicopter Society, Alexandria, VA, May 1994, pp. 1275–1286.

[10] Hariharan, N., and Sankar, L. N., "Application of ENO Schemes to Rotary Wing Problems," AIAA Paper 95-1892, June 1995.

[11] Hall, C. M., and Long, L. N., "High-Order Accurate Simulations of Wake and Tip Vortex Flowfields," *AHS 55th Annual Forum*, American Helicopter Society, Alexandria, VA, May 1999, pp. 1984–1997.

[12] Tang, L., and Baeder, J. D., "Improved Euler Simulation of Hovering Rotor Tip Vortices with Validation," *AHS 55th Annual Forum*, American Helicopter Society, Alexandria, VA, May 1999, pp. 1934–1948.

[13] Hariharan, N., "A First-Principles Based High Order Discontinuous Galerkin (DG) Methodology for Rotorcraft Flowfield Studies," CFD Research Corp., NASA SBIR Phase-I Rept. NAS2-98062, Huntsville, AL, Oct. 1998.

[14] Roe, P. L., "Approximate Riemann Solvers, Parameter Vectors, and Difference Schemes," *Journal of Computational Physics*, Vol. 135, No. 2, Aug. 1997, pp. 250–258. doi:10.1016/0021-9991(81)90128-5

[15] Hariharan, N., and Sankar, L. N., "Unsteady Overset Simulation of Rotor-Airframe Interaction," *Journal of Aircraft*, Vol. 40, No. 4, July–Aug. 2003, pp. 662–675.

[16] Hariharan, N., "Rotary-Wing Wake Capturing: High Order Schemes Towards Minimizing Numerical Vortex Dissipation," *Journal of Aircraft*, Vol. 39, No. 5, Sept.–Oct. 2002, pp. 822–830.